



# Enhanced Vector Field Visualization via Lagrangian Accumulation

Lei Zhang<sup>1</sup>, Duong Nguyen<sup>1</sup>, David Thompson<sup>2</sup>, Robert Laramée<sup>3</sup>, Guoning Chen<sup>1\*</sup>

<sup>1</sup>University of Houston, <sup>2</sup>Mississippi State University, <sup>3</sup>Swansea University

## ARTICLE INFO

### Article history:

Received July 6, 2017

**Keywords:** Vector field visualization, integral curves, aggregation

## ABSTRACT

In this paper, we revisit the *Lagrangian accumulation* process that aggregates the local attribute information along integral curves for vector field visualization. Similar to the previous work, we adopt the notation of the *Lagrangian accumulation field* or  $\mathcal{A}$  field for the representation of the accumulation results. In contrast to the previous work, we provide a more in-depth discussion on the properties of  $\mathcal{A}$  fields and the meaning of the patterns exhibiting in  $\mathcal{A}$  fields. In particular, we revisit the discontinuity in the  $\mathcal{A}$  fields and provide a thorough explanation of its relation to the flow structure and the additional information about the flow that it may reveal. In addition, other remaining questions about the  $\mathcal{A}$  field, such as its sensitivity to the selection of integration time, are also addressed. Based on these new insights, we demonstrate a number of enhanced flow visualizations aided by the accumulation framework and the  $\mathcal{A}$  fields, including a new  $\mathcal{A}$  field guided ribbon placement, an  $\mathcal{A}$  field guided stream surface seeding and the visualization of particle-based flow data. To further demonstrate the generality of the accumulation framework, we extend it to the non-integral geometric curves (i.e., streak lines), which enables us to reveal information about the flow behavior other than those revealed by the integral curves. Finally, we introduce the Eulerian accumulation, which can reveal different flow behaviors from those revealed by Lagrangian accumulation. In summary, we believe that Lagrangian accumulation and the resulting  $\mathcal{A}$  fields offer valuable techniques to investigate flow behavior complementary to the current state-of-the-art techniques.

© 2017 Elsevier B. V. All rights reserved.

## 1. Introduction

Vector field visualization is a ubiquitous technique that is employed to study a wide range of dynamical systems such as automobile and aircraft engineering, climate study, combustion dynamics, earthquake engineering, and medicine, among others. Many effective approaches have been developed to visualize these complex data [1, 2, 3, 4]. There are in general two goals for flow visualization: (1) achieve sufficient spatial cov-

erage and (2) reveal salient flow patterns. The former goal aims to display flow information in possibly every spatial (or spatio-temporal) location to avoid missing important flow behaviors. The latter seeks to identify and display (or highlight) certain important (or salient) flow patterns, in order to reduce the information overloading (i.e., clutter) and occlusion issue. These two goals are some time in conflict with each other, especially when visualizing high-dimensional flows.

Geometric-based visualization is often applied to achieve a tradeoff of the above two conflicting goals. On the one hand, continuous and smooth geometric representations (e.g., integral curves/surfaces) effectively depict the spatio-temporal coher-

\*Corresponding author  
e-mail: [gchen16@uh.edu](mailto:gchen16@uh.edu) (Guoning Chen<sup>1</sup>)

ence nature of vector fields. On the other hand, these geometric representations enable the encoding of flow characteristics in addition to the directional information via color, transparency and texture. To the extreme, full spatial coverage (Goal 1) may be achieved via densely placed integral curves – the intrinsic geometric descriptor of flows, which will certainly result in severe occlusion and clutter. To alleviate these issues, texture-based visualization techniques [5, 6] convolve randomly assigned colors along the integral curves (e.g., streamlines) to introduce enough variance between neighboring streamlines in terms of color to depict the flow patterns in a dense fashion. In a similar spirit, certain accumulated attributes along integral curves have been used to help classify and select integral curves of interest from the densely placed integral curves to reduce the occlusion and clutter in visualization [7, 8, 9, 10, 11]. One example of these techniques is the accumulation of the winding angle along a streamline for the identification of vortex regions [12]. In fact, both the convolution process used in the texture-based visualization and the attribute accumulation in integral curve exploration are essentially accumulations (or aggregations) of quantities along integral curves, a process that we term *Lagrangian accumulation*.

## Problem description.

Zhang et al. [13, 14] recently extended the Lagrangian accumulation to define a derived field based on the accumulated values along integral curves. Briefly, the local flow characteristics along each integral curve are aggregated onto its starting point, allowing the representation of this Lagrangian information (i.e., along integral curves) in an Eulerian fashion (i.e., at their starting points). The derived field, also referred to as the attribute field, denoted by  $\mathcal{A}$ , is used to identify the discontinuity in the behaviors of the neighboring integral curves [13] and perform segmentation of the flow domain [15]. However, there are still a number of unsolved problems with this original Lagrangian accumulation.

First, the characteristics and behaviors of  $\mathcal{A}$  are not well understood. However, it is still not clear exactly what is encoded in  $\mathcal{A}$ . Although there is limited discussion on the potential connection between the discontinuity in  $\mathcal{A}$  and the vector field topology [13], their relationship is yet to be clarified. In addition, the computation of  $\mathcal{A}$  requires the specification of the length of the integration. How this parameter affects the behavior of  $\mathcal{A}$  is unclear. Addressing all of the above questions is crucial to determine under what circumstances that  $\mathcal{A}$  can be useful to assist the tasks of vector field analysis and exploration and how to appropriately utilize  $\mathcal{A}$  without introducing mis-leading information.

Second, it has also been mentioned [13, 14] that different  $\mathcal{A}$ s computed based on different flow characteristics may exhibit different behaviors (or patterns). However, there is no thorough discussion on what characteristics of the vector field the  $\mathcal{A}$  computed from a selected attribute can reveal. Understanding these relationships is important to help the user select the appropriate attribute for the computation of  $\mathcal{A}$ . Furthermore, a

better understanding of the similarity/dissimilarity between  $\mathcal{A}$ s computed using different attributes will provide additional information for the study of the possible causal relations among attributes.

## Our contributions.

To address the above remaining and critical issues, this work makes the following contributions:

- We provide a more in-depth discussion on the properties of  $\mathcal{A}$  fields and the meaning of the patterns exhibiting in  $\mathcal{A}$  fields. In particular, we revisit the discontinuity in the  $\mathcal{A}$  fields and provide a thorough explanation of its relation with the flow structure and the additional information that it may reveal. Other remaining questions about the  $\mathcal{A}$  fields, such as its sensitivity to the selection of integration time, are also discussed. (Section 4)
- We propose a number of enhanced flow visualizations aided by  $\mathcal{A}$  fields, including a new  $\mathcal{A}$  field-guided ribbon placement, an  $\mathcal{A}$  field-guided stream surface seeding and the visualization of particle-based flow data. We have applied these enhanced visualizations to a number of 2D/3D steady/unsteady flow data. (Section 5.1)
- We provide an informal study of the relationship among different attributes, which we hope may enlighten the selection of appropriate attributes for accumulation to meet different needs. (Section 5.2)
- We extend the previous accumulation defined along integral curves to a non-integral geometric curve (i.e., streak lines), which enables us to reveal information about the flow behavior different from those revealed by accumulating along integral curves. (Section 5.3)
- Finally, we introduce Eulerian accumulation for unsteady flow data, which aggregates the local attribute information at fixed spatial locations over time. This enables us to inspect the flow from a different perspective than the Lagrangian accumulation. (Section 5.4)

In summary, we believe the Lagrangian accumulation (or the general accumulation) and the resulting  $\mathcal{A}$  fields offers a valuable way to support the exploration of flow behaviors in addition to the current state-of-the-art techniques.

## 2. Related Work

There is a large body of literature on the analysis and visualization of flow data. Interested readers are encouraged to refer to recent surveys on the dense and texture-based visualization techniques [5], geometric-based methods [16], illustrative visualization [17], topology-based methods [2, 3], and partition-based techniques [4], respectively. In this section, we focus on the most relevant work.

**Dense and texture-based techniques** Dense and texture-based flow visualization techniques have been among the most popular methods that aim to reveal the flow directional information,

while simultaneously achieving full spatial coverage. Based on the survey [5], texture-based techniques can be classified into line integral convolution (LIC) techniques [18, 19, 20, 21, 22] and advection (or warping) based techniques [23, 24, 25]. The goal of both groups is to make the output image have similar color along integral curves, but with varying color along the direction that is perpendicular to the flow direction. Matvienko and Kruger [6] utilized this observation to study the inequality property of the generated texture images to evaluate their quality. In this work, we study a similar inequality property of the resulting  $\mathcal{A}$  fields computed by accumulating along integral curves. In the meantime, dense visualization can be generated by measuring the density of the integral curves within any spatial unit, such as the structure-accentuating dense flow visualization [26]. The obtained salient flow structure is typically located around separation structures due to the strong convergence of flow there. In this work, we discuss how this varying density of the integral curves in the flow domain may influence the salient structure encoded in the  $\mathcal{A}$  field.

**Lagrangian framework for flow analysis** In fluid dynamics, there are two different views for the study of flow behaviors, i.e., observing the flow at fixed location—Eulerian point of view, or observing it on a moving particle—Lagrangian point of view. In this work, we specifically focus on the Lagrangian framework, which studies the behavior of particles along their individual paths, i.e., integral curves computed from the seeded positions. According to this characteristic, the Finite-Time Lyapunov Exponent (FTLE) [27], the streamline [9] and pathline [10] predicates, the pathline attribute approaches [8, 11, 28], and the streamline and pathline dissimilarity for streamline clustering [29], selection [30], and the ensemble analysis [31] are all examples of Lagrangian approaches. Among these, the FTLE approach aims to measure the rate of flow separation at individual spatial sampling points. Its flow map computation is essentially a special case of Lagrangian accumulation (Section 3.2) that sums up all the vector values starting from an initial point scaled by the integration step size along the path of the particle, which leads to the end position of a particle. This accumulation neglects all intermediate positions as well as other information about the particle that is not relevant to the flow separation. The computed rate of separation at each point is encoded as a scalar field, which facilitates the identification of its ridges—known as the Lagrangian Coherent Structure (LCS). This Eulerian representation of the FTLE fields is similar to our derived  $\mathcal{A}$  fields. Nonetheless, the Lagrangian accumulation and the resulting  $\mathcal{A}$  fields are more general than the FTLE approach, and can be used to encode attributes of the particles along their paths rather than just at their starting and ending positions.

The idea of accumulating local characteristics along the particle trajectories and assigning the accumulated values to the corresponding integral curves has been applied using the pathline attribute approaches. Specifically, Shi et al. [11] presented a data exploration system to study the different characteristics of pathlines based on their various attributes. Pobitzer et al. [8] applied

a statistics-based method to select a proper subset of pathline attributes to improve the interactive flow analysis. While not directly accumulating the local attributes, Guo et al. [28] proposed to accumulate the square difference between the local attributes along pairs of integral curves to define the distance between them. Recently, Zhang et al. [13, 14] extended the above Lagrangian accumulation to define an attribute field based on the accumulated values along integral curves. This attribute field adopts the Eulerian representation of the Lagrangian information, in a similar fashion to the texture-based technique, which enables a continuous representation of the variation of the integral curve behaviors to some extent. In contrast to the previous work by Zhang et al., we provide a deeper discussion on the behaviors of the obtained attribute fields and extend the Lagrangian accumulation to the accumulation along non-integral curves (i.e. streak lines). Furthermore, we introduce an Eulerian accumulation framework.

More recently, Lagrangian representation has been introduced to address the scalability issue of the visualization of large scale unsteady flows [28, 32].

### 3. The Lagrangian Accumulation

In this section, we describe the Lagrangian accumulation and provide an in-depth discussion on its behavior under different selections of parameters. We also offer a thorough discussion on what can be revealed in the derived attribute fields from the accumulation. In the following, we start with a brief review of some important concepts of vector fields.

#### 3.1. Vector Field Background

Consider a spatial domain  $\mathbb{D} = \mathbb{M} \times \mathbb{R} \subset \mathbb{R}^3$ . A general vector field can be expressed as an ordinary differential equation (ODE)  $\dot{\mathbf{x}} = \mathbf{v}(\mathbf{x}; t)$ . An integral curve (or trajectory) that is everywhere tangent to  $\mathbf{v}$  is a solution to the initial value problem of the above ODE system, denoted by  $\mathbf{x}(t) = \mathbf{x}_0 + \int_0^t \mathbf{v}(\mathbf{x}(\tau); t_0 + \tau) d\tau$ . In unsteady vector fields, an integral curve is also referred to as a pathline, while in the steady case, it is called streamline. There are a few special streamlines in steady flows. Streamlines that degenerate to points are fixed points. They correspond to locations where  $\mathbf{v} = 0$ . Streamlines that form closed curves are referred to as periodic orbits, together with fixed points, they define the vector field topology [33].

**Flow Attributes.** Given a vector field  $\mathbf{v}$ , its spatial gradient  $\nabla_{\mathbf{x}}\mathbf{v}$  is referred to as its *Jacobian*, denoted by  $\mathbf{J}$ .  $\mathbf{J}$  can be decomposed as  $\mathbf{J} = \mathbf{S} + \mathbf{R}$ , where  $\mathbf{S} = \frac{1}{2}[\mathbf{J} + (\mathbf{J})^T]$  and  $\mathbf{R} = \frac{1}{2}[\mathbf{J} - (\mathbf{J})^T]$  are the symmetric and antisymmetric components of  $\mathbf{J}$ , respectively. A number of flow attributes can be derived from  $\mathbf{v}$ ,  $\mathbf{J}$ ,  $\mathbf{S}$  and  $\mathbf{R}$  [8]. In this work, we utilize the following local attributes,  $a_i$ , for various experiments.

- $a_1$ : vorticity,  $\|\nabla \times \mathbf{v}\|$ .
- $a_2$ : divergence,  $tr(\mathbf{J})$ , i.e., trace of  $\mathbf{J}$ .

- $a_3$ : helicity,  $\nabla \times \mathbf{v} \cdot \mathbf{v}$ .
- $a_4$ :  $\lambda_2$ , the second largest eigenvalue of the tensor  $\mathbf{S}^2 + \mathbf{R}^2$  [34].
- $a_5$ :  $Q = \frac{1}{2}(\|\mathbf{R}\|^2 - \|\mathbf{S}\|^2)$  [35].
- $a_6$ : local shear rate, the Frobenius norm of  $\mathbf{S}$ .
- $a_7$ : determinant of  $\mathbf{J}$ .
- $a_8$ : change of flow direction (also known as winding angle),  $\angle(\mathbf{v}(\mathbf{p}_i), \mathbf{v}(\mathbf{p}_{i+1}))$  where  $\mathbf{p}_i$  denotes a point on an integral curve. This geometric attribute essentially measures the curvature of the integral curve at  $\mathbf{p}_i$ .
- $a_9$ : velocity vector  $\mathbf{v}$ .
- $a_{10}$ : acceleration,  $\mathbf{a}(\mathbf{x}, t) = \frac{D\mathbf{v}}{Dt} = \frac{\partial \mathbf{v}(\mathbf{x}, t)}{\partial t} + (\mathbf{v}(\mathbf{x}, t) \cdot \nabla) \mathbf{v}(\mathbf{x}, t)$ .

### 3.2. Lagrangian Accumulation of Local Attributes

Consider an integral curve,  $\mathcal{C}$ , starting from a given point  $(\mathbf{x}, t_0)$ , the Lagrangian accumulation can be formulated as the following convolution process.

$$A_g((\mathbf{x}, t_0), t) = \int_0^t k(\tau) a_l(\mathcal{C}(\tau), t_0 + \tau) d\tau \quad (1)$$

where  $k(\tau)$  is a filter kernel following the integral curves [18, 25]. For simplicity, in this work we assume a simple *box filter* [21], for all examples.  $a_l(\mathcal{C}(\tau), t_0 + \tau)$  is the value of the selected local flow property  $a_l$  measured at location  $\mathcal{C}(\tau)$  and at time  $t_0 + \tau$ , which can be either scalar, vector, or tensor values. For the later discussion, we mainly consider scalar properties. In most cases,  $a_l$  is continuous in  $\mathbb{D}$  except at some special locations, such as fixed points in the steady cases.  $A_g((\mathbf{x}, t_0), t)$  represents the accumulated value.  $t \in \mathbb{R}$  is the integration window size. Note that  $t$  can be negative to account for the backward integration. In addition, considering both forward and backward integration starting at  $(\mathbf{x}, t_0)$  is also possible. Nonetheless, we will concentrate on the forward integration for now.

The above formulation describes accumulation under time-dependent conditions. In steady cases, the local attribute values are not dependent on the current integration time but only the location, i.e., denoted by  $a_l(\mathcal{C}(\tau))$ . More often, in the steady cases, the accumulation is performed with a specified length  $s$  along the streamlines.

$$A_g(\mathbf{x}, s) = \int_0^s k(\eta) a_l(\mathcal{C}(\eta)) d\eta \quad (2)$$

Again, this accumulation along a streamline can also be performed in both forward and backward directions. To simplify the subsequent discussion, we will refer to the Lagrangian accumulation as the *L-accumulation* for the rest of the paper.

Given a spatio-temporal domain  $\mathbb{D} = \mathbb{M} \times \mathbb{T}$ , a derived scalar field can be obtained (assuming  $a_l$  is scalar) from the above convolution, where the value at each sample position is determined by Eq.(1) or (2). We refer to this field as a Lagrangian Accumulation field or an  $\mathcal{A}$  field. The scalar fields discussed in [36] are essentially examples of  $\mathcal{A}$  fields. Given different local characteristics to accumulate, one can obtain various  $\mathcal{A}$

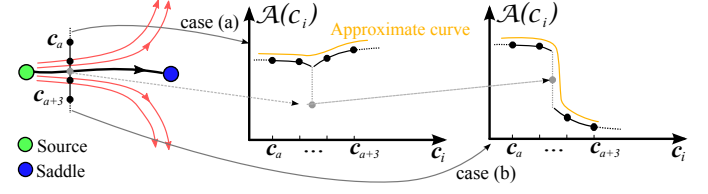


Fig. 1: Discontinuity of the  $\mathcal{A}$  field at a separatrix connecting a saddle (blue dot) and a source (green dot). The  $\mathcal{A}$  field is sampled along the line segment traversing through the separatrix.  $c_i$  indicate the samples along this segment. Case (a) shows a scenario of the discontinuity that the discrete sampling may miss (illustrated by the orange curve), while the discontinuity in case (b) could be captured with sufficient samples.

fields. A discussion on the relationships between some of these  $\mathcal{A}$  fields is provided in a later section. Given an  $\mathcal{A}$  field and its gradient,  $\nabla \mathcal{A}$ , the gradient magnitude can be computed and used to identify locations where the  $\mathcal{A}$  field has large changes.

### 4. Properties of $\mathcal{A}$ Fields

It has been previously noted that there are a number of important properties of  $\mathcal{A}$  that make it suitable for a number of flow exploration tasks. However, among these properties, the discontinuity in  $\mathcal{A}$  still lacks a thorough and informative discussion, leading to concerns about the interpretation of the information provided by this discontinuity. In this section, we attempt to resolve this concern.

**Uniqueness** Given the above definition of the  $\mathcal{A}$  field, it is apparent that given any point  $(\mathbf{x}, t) \in \mathbb{D}$  (except at fixed points in steady flows), there is exactly one  $\mathcal{A}$  value with the specified integration time or length. This is due to the uniqueness of integral curves, i.e., in theory there exists exactly one integral curve passing through any given point except at fixed points. This property allows  $\mathcal{A}$  field to achieve full spatial coverage without ambiguity except at fixed points.

**Inequality** Since neighboring points that are correlated by the same integral curves may have similar values, the following inequality is expected to hold for the accumulation, as pointed out by Matvienko and Kruger [6].

$$|\langle \nabla \mathcal{A}, \mathbf{v}^\perp \rangle| > |\langle \nabla \mathcal{A}, \mathbf{v} \rangle|$$

However, due to the influence of different integration times (or lengths), as discussed later, we observe a weaker inequality in practice as below

$$|\nabla \mathcal{A}| > |\langle \nabla \mathcal{A}, \frac{\mathbf{v}}{\|\mathbf{v}\|} \rangle|$$

This inequality property shows that the patterns observed in  $\mathcal{A}$  fields are mostly aligned with the flow direction except at places where  $\mathcal{A}$  exhibits certain discontinuous behaviors.

#### 4.1. Revisit the Discontinuity in $\mathcal{A}$

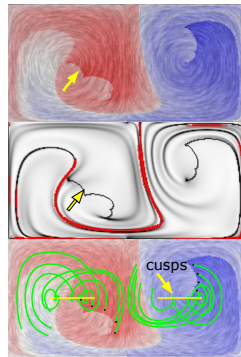
In mathematics, a function  $f(\mathbf{x})$  defined in  $\mathbb{M}$  is said to be continuous at  $\mathbf{c}$  if for every  $\varepsilon > 0$ , there exists a  $\delta > 0$  such that for



all  $\mathbf{x} \in \mathbb{M} \mid |\mathbf{x} - \mathbf{c}| < \delta \Rightarrow |f(\mathbf{x}) - f(\mathbf{c})| < \varepsilon$ . However, this condition may not be satisfied everywhere in  $\mathbb{D}$  by a  $\mathcal{A}$  field. Specifically, for a steady vector field that consists of fixed points, the integral curves (or streamlines) passing through them reduce to points. Therefore, the obtained  $\mathcal{A}$  field is not well-defined (i.e., it is discontinuous) there.

The second place where  $\mathcal{A}$  may exhibit discontinuous behavior is at separation structures in the flow. Consider a smooth vector field, the transition of the (geometric) behaviors of neighboring integral curves is smooth. However, this smooth transition is violated at locations where the integral curves have structural changes (e.g., end at different fixed points or two far away locations). Those locations correspond to the separation structures in the flow. In many cases, especially in unsteady vector fields, these separation structures are not unique and are sensitive to the selection of the integration time (see the later discussion on this). In contrast, vector field topology provides a rigorous description of the separation structures of steady vector fields, which are defined in an infinitely long time. In either case, this geometrically discontinuous behavior of integral curves may or may not be reflected by the  $\mathcal{A}$  fields that accumulate the local characteristics along integral curves. Figure 1 shows two cases where the  $\mathcal{A}$  field misses (a) or captures (b) the topological discontinuity across a separatrix. In case (a), the accumulation values on both sides of the separatrix are similar despite different geometric behaviors of their associated streamlines. Depending on the seeding location and possibly numerical error, this discontinuity may be missed. In case (b), the accumulation values on both sides are sufficiently different, capturing the discontinuous geometric behavior across the separatrix.

Does this mean that the discontinuity exhibited in  $\mathcal{A}$  is always a subset of the separation structures of the vector fields? To answer this question, let us look at another example shown in the inset to the right. This example shows an  $\mathcal{A}$  computed by accumulating the change of the flow direction along the densely placed pathlines for the Double Gyre flow. Besides the well-known separation structure defined as the ridges of the so-called FTLE field, there exists additional discontinuity in the computed  $\mathcal{A}$  as highlighted by the arrows. By a close inspection, this cusp-like discontinuity is caused by the abrupt directional change in the integration of the involved pathlines due to the two oscillating centers. This behavior has already been reported in a previous work [37]. This example indicates that the discontinuity in  $\mathcal{A}$  may correspond to the discontinuous behaviors of neighboring pathlines other than their geometric characteristics.



Based on the above discussion and analysis, we can conclude that, under the numerical error free assumption, the discontinuity exhibited in  $\mathcal{A}$  indeed corresponds to the discontinuous geometric and/or physical behaviors of neighboring integral curves. However, not all discontinuities can be captured by  $\mathcal{A}$

in practice due to the selection of integration times and seeding strategy. With this observation, we argue that the accumulation framework and the resulting  $\mathcal{A}$  fields are a simple and effective means to provide an approximate overview of the potential discontinuity in integral curve behaviors, which is known to be relevant to a number of important flow features.

**Remark:** The highlighted discontinuity in  $\mathcal{A}$  may not provide the precise locations and times where and when it happens. Recall the example shown in the above inset. Although the sharp direction change occurs in a later time in the flow, the discontinuity occurs in the first time step where those pathlines are seeded. Although this looks like a disadvantage of the accumulation framework and  $\mathcal{A}$  fields, it indeed provides a robust way for the seeding and selection of integral curves that may possess interesting behaviors (i.e., the abrupt change of direction) without extracting those features precisely. Nonetheless, there are still cases that knowing the exact local spatio-temporal regions where those features/events occur is necessary. In that case, additional information needs to be utilized to complement the accumulated value. One possible solution is to study the variation and distribution of the local attributes along integral curves to provide more detailed information about integral curve behaviors, which should be a valuable future direction.

**Sensitivity to integration time/length** The definition of  $\mathcal{A}$  is unfortunately sensitive to the specified integration time/length. That means that different  $\mathcal{A}$ s computed with different integration times/lengths may exhibit different patterns (i.e., different discontinuity structures). Figure 2 provides an example showing the  $\mathcal{A}$  fields based on the accumulation of the change of flow direction (aka. signed curvature) of a simple separation flow with different integration times/length. From the results, we see that, with a smaller integration length (Figure 2 a), the  $\mathcal{A}$  field tends to capture the local and short-term flow behaviors. Interestingly, it identifies locations with large flow curvature. In contrast, a longer integration length may reveal the global and long-term flow behaviors (Figure 2 b), and produce smoother  $\mathcal{A}$  fields at the same time. This effect is similar to the behavior observed in the convolution process used by the texture-based techniques [6]. Figure 2 (c) shows the plots of the  $\mathcal{A}$  values along two line segments (shown in Figure 2 (b)). As can be seen, the ranges of the  $\mathcal{A}$  values on these two sampled segments are not identical. This again can be attributed to the sensitivity of the sampling location on the separation structure and the smeared effect of long integration. In practice, the selection of the integration times/lengths depends on the needs of the applications. If the local characteristic of the flow is of interest, a small integration time can be selected, while if the global and structure information of the flow is the focus, a long integration may be used. A similar consideration on the selection of integration time can be seen in the FTLE computation.

**Average of the accumulated value** To avoid the artifacts introduced by the number of integration steps, especially when the integral curves are approaching fixed points, we also com-

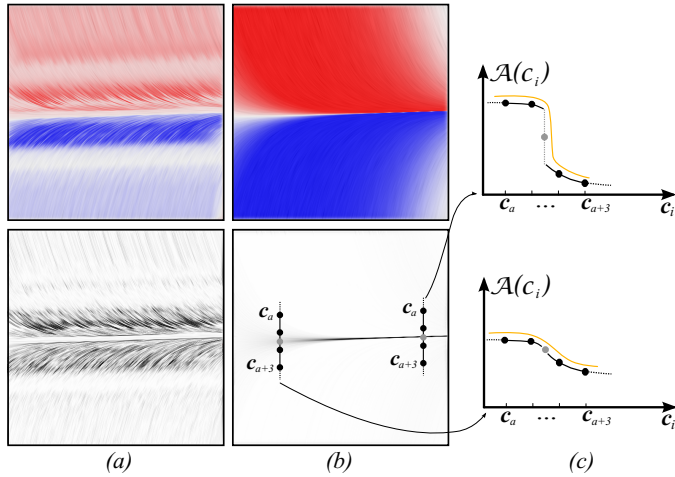


Fig. 2: The influence of the accumulation window size (i.e integration length). (a) shows the  $\mathcal{A}$  field computed with the integration length equal 10% of the size of the bounding box of the flow domain, while (b) shows the  $\mathcal{A}$  field with the length equal twice of the size of the bounding box. (c) shows the plots of the  $\mathcal{A}$  values sampled along two seeding line segments. As can be seen, even they have the same length, the two segments encode different amount of information quantified by the range of the  $\mathcal{A}$  values along the segments.

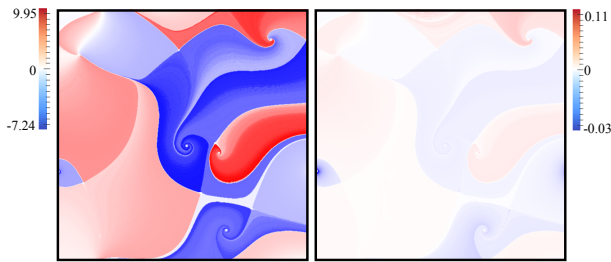


Fig. 3: The  $\mathcal{A}$  fields computed without (left) and with average (right).

puted  $A'_g(\mathbf{x}, t) = \frac{1}{t} A_g((\mathbf{x}, t_0), t)$  for unsteady flow and  $A'_g(\mathbf{x}, s) = \frac{1}{s} A_g(\mathbf{x}, s)$  for steady flow, which essentially describes the average behavior of the particle along its path. We compare the resulting  $\mathcal{A}$  fields with and without this average computation and observe that they in general have similar behavior with the difference of some scalar factor (Figure 3). The benefit of using the average value is that it enables us to inspect the overall attribute behavior along the integral curves. This can be useful when studying the behaviors of particles in unsteady flows. However, the difference between the  $\mathcal{A}$  values near the discontinuity tends to become smaller (Figure 3(right)), which may make the identification of these places challenging. Therefore, in most of our experiments, we use the non-average version of the  $\mathcal{A}$  fields.

## 5. $\mathcal{A}$ Field Enabled Flow Exploration and Discussion

Based on the above discussions on the properties of  $\mathcal{A}$  fields, we now describe how to utilize accumulation to support a number of flow visualization and exploration tasks. Previous work has demonstrated that the obtained  $\mathcal{A}$  fields can be used to assist the seeding and selection of integral curves and perform flow segmentation. In this section, we demonstrate how to use

$\mathcal{A}$  fields and other information derived from the local attributes to perform ribbon and stream surface placement for 3D flow visualization. In addition, we show a new application of  $\mathcal{A}$  fields in the visualization of particle-based flow data. Furthermore, we will provide an informal discussion on the relationships between certain attributes in terms of the behaviors of their corresponding  $\mathcal{A}$  fields, followed by a couple of extensions of the accumulation framework.

**Compute  $\mathcal{A}$  in practice** The general computation framework for  $\mathcal{A}$  has been described in [13]. For completeness, we briefly describe this framework. We use a uniform dense sampling strategy to avoid any bias under the assumption that no prior knowledge of the data is available. Given any sample point, an integral curve (i.e., a streamline for a steady vector field or a pathline for an unsteady vector field) is computed using the standard Runge-Kutta fourth order integrator (RK4) with a fixed step size. The local attribute values are interpolated at the integration points based on the pre-computed values at the uniform dense samples. It is worth noting that due to the uniform sampling strategy and an axis dependent order, the computed  $\mathcal{A}$  may possess certain artifacts or numerical errors. To address this, we introduce two additional processes to the original accumulation framework. First, we construct a dual grid with the uniform samples as the centers of the grid cells. For each grid cell, a list of the computed integral curves passing through it is recorded. As long as a cell is traversed by an integral curve, this cell is marked visited, and its  $\mathcal{A}$  value is computed as the weighted sum of the  $\mathcal{A}$  values of the integral curves passing it. The weights are selected based on their distance to the center of the cell. Second, after obtaining the initial  $\mathcal{A}$  field, we further smooth it along the flow direction in a similar fashion of the enhanced-LIC approach [38]. That is, we perform another low-pass filtering process along the short integral curves seeded at the sampling points with the  $\mathcal{A}$  field as the input. This additional smoothing can be very usefully in cases in which the samples are irregular (i.e., the vertices of the triangle mesh), which is typical for surface flows. Figure 4 provides a few examples of the  $\mathcal{A}$  fields computed on triangle meshes. In these examples, the streamlines are seeded at the individual vertices of the triangular meshes and integrated for a sufficiently long period (e.g. twice the size of the bounding box of the geometry). Figure 4(a, left) shows the initial accumulated  $\mathcal{A}$ , which is not smooth. After performing the aforementioned smoothing, the  $\mathcal{A}$  is better aligned with the flow (Figure 4(a, right)). The computation times for  $\mathcal{A}$  fields depend on the size of the data, the resolution of the samples and the integration time, which can range from a few seconds (e.g., the 2D steady flow) to 2 hours (e.g., the surface flows) on a PC with an Intel Xeron 1.6GHz CPU and 8GB RAM without any parallelization.

### 5.1. Enhanced Flow Visualization with the Aid of $\mathcal{A}$

In this section, we demonstrate how to utilize the computed  $\mathcal{A}$  and its properties to achieve a number of enhanced visualization for the exploration of various flow data.

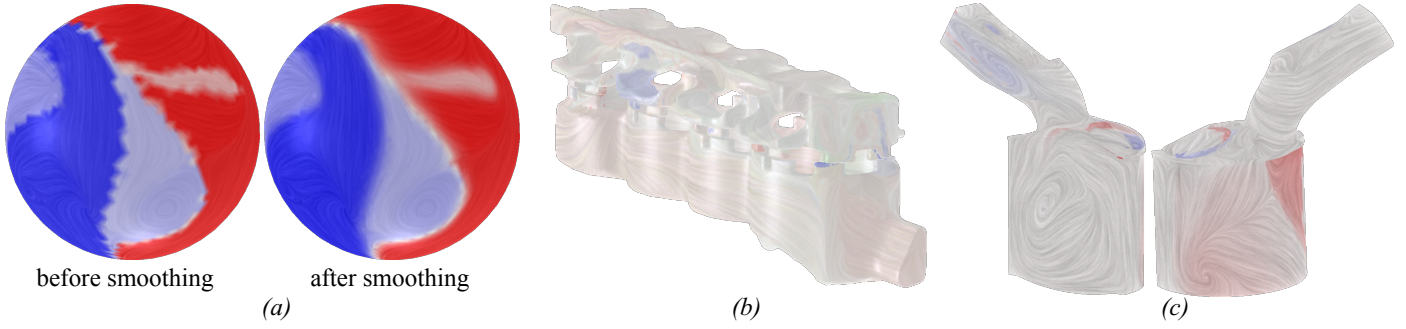


Fig. 4:  $\mathcal{A}$  fields of a synthetic surface flow (a), a cooling jacket simulation (b) and a gas engine simulation (c), respectively.

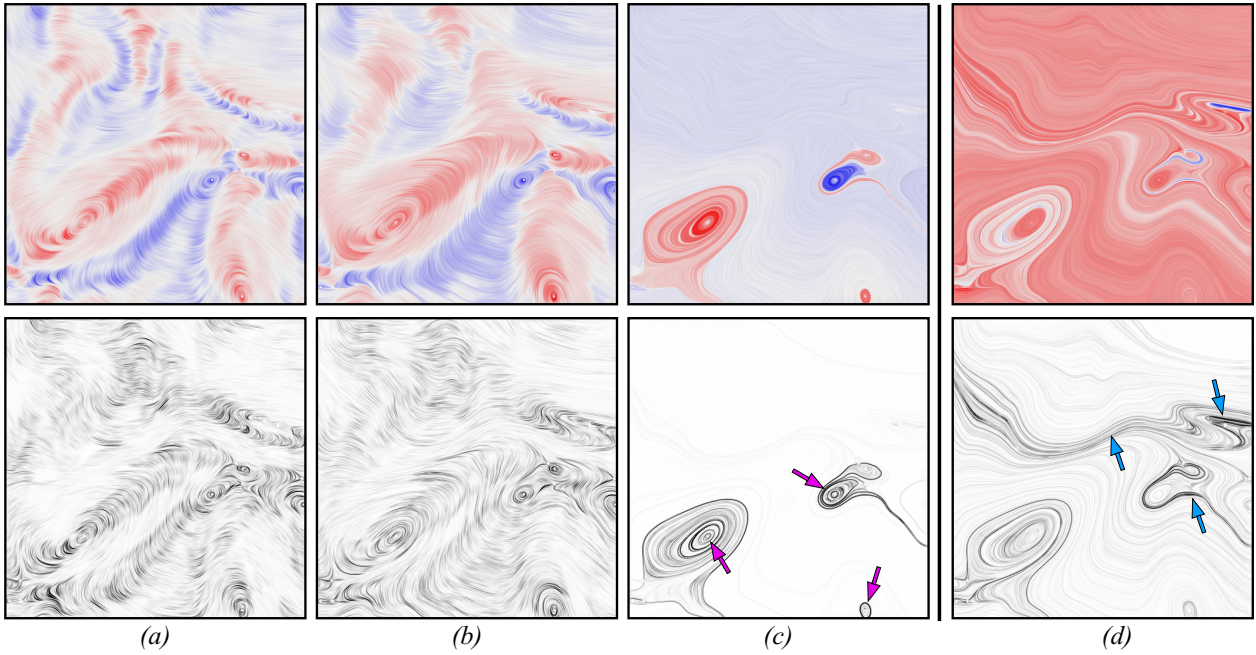


Fig. 5:  $\mathcal{A}$  (top) and  $|\nabla \mathcal{A}|$  (bottom) fields of a tile of the ocean simulation with different window sizes for accumulation. (a) 10% of the size of the bounding box of the data domain; (b) 50%; (c) 2,000%. (d) shows the  $\mathcal{A}$  field by accumulating the local attribute divergence ( $a_2$ ) along streamlines.

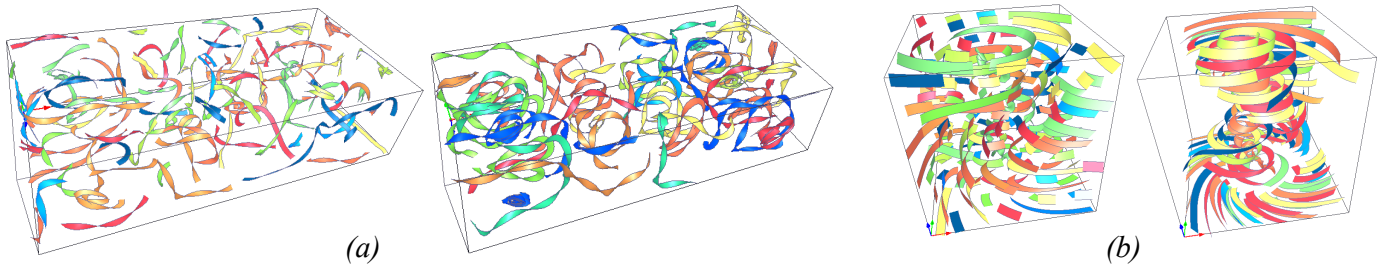


Fig. 6: Ribbon placement results for the Bernard data (a) and the tornado data (b), respectively. The left image of each group shows the ribbon placement guided by local helicity information, while the right image shows the placement guided by the derived  $\mathcal{A}$  field based on the local attribute helicity ( $a_3$ ).

### 5.1.1. Directly Visualizing $\mathcal{A}$ and $|\nabla \mathcal{A}|$

Figure 5 illustrates how to utilize the  $\mathcal{A}$  and  $|\nabla \mathcal{A}|$  fields computed with different accumulation window sizes for the creation of visualizations with different styles. A tile at a specific time from the surface layer of an ocean simulation data [39] is used. We accumulate the curl of the flow to compute the  $\mathcal{A}$  fields shown in Figure 5 (a-c). A  $512 \times 512$  uniform sampling strategy is used. From these results, we see that with a small ac-

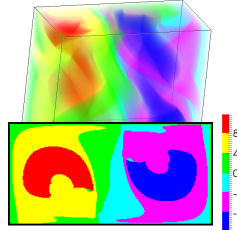
cumulation window size, e.g., 10% of the size of the bounding box of the domain, the resulting  $\mathcal{A}$  field is not smooth and possesses patterns that are short but are aligned with the flow, when compared to the background LIC(a, top). Its discontinuity estimated by the  $|\nabla \mathcal{A}|$  field generates a visualization similar to LIC but also highlighting locations that have stronger local rotation. With a sufficiently large window, e.g., twenty times the size of the bounding box, the resulting  $\mathcal{A}$  is smoother, and its discontinuity tends to be located around a few vortices in the flow.



Figure 5(d) shows an  $\mathcal{A}$  field computed by accumulating the divergence along the streamlines of the same flow. The window size for accumulation is twenty times the size of the bounding box. Compared to the result shown in (c), the divergence-based  $\mathcal{A}$  field tends to highlight the spatial positions with strong separation behavior as expected. Additional results can be found in the supplemental document.

### Pseudo segmentation via discrete color coding

With the spatial coverage property and the inequality property that makes the patterns in the  $\mathcal{A}$  field align with the flow direction, one can easily create a visualization using a discrete color coding to achieve an effect similar to a flow domain segmentation. The inset provides an example of a discrete color visualization. Note that no actual segmentation is performed in this visualization. However, a true segmentation may be obtained with this discrete color assignment as the input [15].



**Remarks:** We wish to emphasize that it is because the patterns of the  $\mathcal{A}$  fields are aligned with the flow except at fixed points, the direct visualization of  $\mathcal{A}$  and  $\nabla\mathcal{A}$  fields often provide us an overview of the flow behavior. However, one should also appreciate the sensitivity of the  $\mathcal{A}$  fields w.r.t the integration times, which may reveal local or global behaviors of the flow in different scales.

### 5.1.2. An $\mathcal{A}$ Field Guided Ribbon Placement

3D ribbons are known good for representing flow characteristics that neither integral curves nor integral surfaces can effectively convey. One example is the helicity of the flow, which characterizes the rotational behavior around an integral curve. To utilize this information to guide the seeding and placement of ribbons, we first aggregate the helicity along the individual streamlines to obtain an  $\mathcal{A}$ . Then we derive the standard deviation of the helicity values along each streamline, denoted by  $\sigma$ . For each candidate seed  $\mathbf{p}$ , we assign a value of  $\mathcal{A}(\mathbf{p}) + \sigma(\mathbf{p})$ . Based on this value, we rank all candidate seeds that are uniformly distributed in  $\mathbb{D}$ . From the top-ranked seeds, we construct a series of ribbons as the initial set of ribbons. Then, we iteratively insert new ribbons that fill the blank region of  $\mathbb{D}$  while keeping a minimum, user-specified distance away from other existing ribbons. The similarity metric introduced by Chen et al. [40] is used to further remove redundant ribbons that are too similar to the existing ones. Figure 6 shows the ribbon placement results using the proposed  $\mathcal{A}$  field guided framework. Compared to the ones that are produced using only the local attributes (i.e., the initial ribbons are placed at locations with maximum local attribute values), our results tend to generate ribbons with longer length that can provide more coherent information about the flow behaviors (i.e., the tornado and the four vortices of the Bernard data are easily identifiable), which

is expected.

### 5.1.3. An $\mathcal{A}$ Field Guided Surface Seeding

An integral surface is the integration of a 1D curve (i.e., seeding curve) through 3D flows. Compared to individual integral curves, integral surfaces can more effectively convey 3D flow information by incorporating additional visual cues (e.g., lighting, transparency and textures). However, not all integral surfaces are intrinsic. They highly depend on the selection of the seeding position and the shape and orientation of the seeding curve. Generating good seeding curves that leads to expressive surface representation of the flow is still a challenging task. With the computed  $\mathcal{A}$  and its gradient information, we develop a simple yet effective seeding curve generation strategy. In particular, we select a candidate seed  $\mathbf{p}_c$  that has the smallest  $|\nabla\mathcal{A}|$  value. Let us denote the  $\mathcal{A}$  value at  $\mathbf{p}_c$  by  $g$ . Next, we generate a seeding curve starting from  $\mathbf{p}_c$  and guided by the curvature field [41], whose points have  $\mathcal{A}$  values falling in the range  $[g - \delta, g + \delta]$ . The obtained seeding curve encodes streamlines, for which the variation of  $\mathcal{A}$  values is not larger than  $\delta$ . Thus, the computed stream surface from this seeding curve is expected to have small variation of behaviors. In the meantime, we can select a candidate seed  $\mathbf{p}'_c$  that has the largest  $|\nabla\mathcal{A}|$  value, from which we generate a seeding curve guided by the  $\nabla\mathcal{A}$  field. The computed stream surface from this seeding curve is expected to have large variation according to the meaning of the  $\nabla\mathcal{A}$  field (i.e., it highlights the places where  $\mathcal{A}$  has large changes). Figure 7 shows two surfaces computed from the two seeding curves constructed using the above two strategies for the flow behind the cylinder data, respectively. The blue surface was generated from a seeding curve with small variation of  $\mathcal{A}$  values along it, which highlights the boundary of a small vortical region next to the cylinder object. In contrast, the red surface was generated from a seeding curve with large variation in the  $\mathcal{A}$  values. This surface exhibits rich and varying flow behaviors around the boundaries of various vortices.

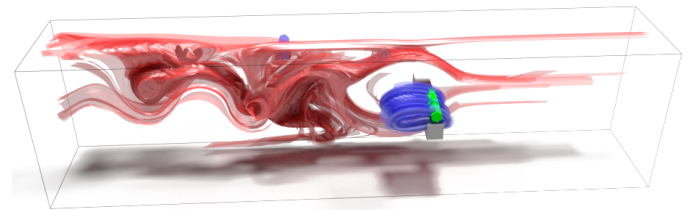


Fig. 7: Comparison of two strategies of seeding curve generation. The red surface is constructed from a seeding curve derived using the small variation strategy, while the yellow is from a seeding curve derived using the large variation strategy. The seed of seeding curve for the blue surface is located inside the bundle, where its  $|\nabla\mathcal{A}|$  value is small, i.e., the  $\mathcal{A}$  values along this seeding curve are almost constant. In contrast, the seed position of the seeding curve for the red surface is located near the boundary of the domain, where the  $|\nabla\mathcal{A}|$  value is large, and the variation of the  $\mathcal{A}$  values on this seeding curve is also large.

### 5.1.4. Visualizing Particle-based Data Aided by $\mathcal{A}$

In addition to applying the accumulation framework to mesh-based vector field data, we also utilize it to aid the visual ex-

ploration of the particle-based flow data. In contrast to the previous examples in which the integral curves are computed to depict the trajectories of mass-less particles, the particles in the particle-based data have mass and their trajectories need not be the integral curves of the corresponding velocity field. Nonetheless, the accumulation framework still applies. In this case, the accumulated value of a particle indeed describes the overall attribute behavior of the particle. Figure 8 shows an  $\mathcal{A}$  field computed based on the change of the moving direction (i.e.,  $a_8$ ) of the particles produced by a dam-breaking simulations computed using the position-based fluid method [42]. From the result we see that particles that hit the boundary have larger change of moving direction, as highlighted by the arrows

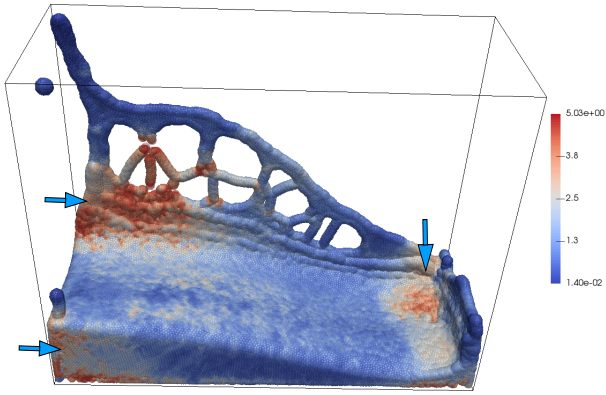


Fig. 8: Visualization of an  $\mathcal{A}$  field derived from a dam-breaking particle based simulation using local attribute  $a_8$ . Blue means the change of particle moving direction is small, while red means large. It shows that the particles that hit the boundary have larger change of moving direction, as highlighted by the arrows.

## 5.2. An Informal Study of Relation Among Attributes

In this section, we conduct an informal study of the relationships between a number of selected geometric characteristics of the integral curves and their corresponding flow properties.

**Arc-length vs. velocity magnitude** It is not surprising that these two properties are directly related, as the arc-length of each segment of an integral curve is determined by the length of the vector value at the starting point of this segment scaled by the integration step size, i.e., scaled velocity magnitude.

**Winding angle vs. curl** Figure 9(a-c) shows a comparison of two  $\mathcal{A}$  fields computed by accumulating the change of the flow direction, i.e., winding angle (top) and curl (bottom) for some 2D flows, respectively. As can be seen, they exhibit almost identical patterns in the steady case (a-b), even though they quantify flow rotational behaviors differently – curl quantifies the amount of rotation of the flow, i.e., twice the angular velocity, around a point in the flow domain, while winding angle measures the amount of turning at a point on an integral curve by computing the angle difference of the vectors at two consecutive points on the curve. Nonetheless, in general the curl-based  $\mathcal{A}$  fields tend to be smoother than the winding angle based  $\mathcal{A}$  fields. This is because the curl at any given integration point is obtained via interpolation during the accumulation, while the angle difference between flow vectors is estimated via the angle

change of the orientation of the two consecutive line segments of the integral curve, which is subject to numerical error. However, curl-based  $\mathcal{A}$  fields may not be able to capture some discontinuities in the geometric behaviors of the integral curves. As shown in Figure 9(c), the cusp-like behavior of pathlines (highlighted by the arrows) is not captured by the curl-based  $\mathcal{A}$  field. This is because the cusp-like behavior corresponds to a sharp angle (i.e.,  $\pi$ ) change which makes the flow directions before and after the cusp nearly pointing in opposite directions, i.e., they are almost co-linear. Thus, the discrete curl computation that is performed while the cross product computation will return zero or a very small value. Nonetheless, the relationship between curl and the change of flow direction, as well as among other vortex identification criteria, such as  $\lambda_2$  and  $Q$ , should be systematically studied to solve the problem of the current lack of a unified definition of a vortex.

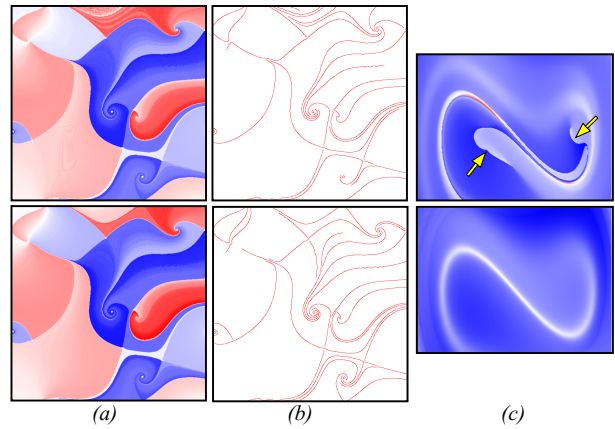


Fig. 9: Comparison of the  $\mathcal{A}$  fields computed by accumulating the curl  $a_1$  (bottom) and the change of the flow direction  $a_8$  (top), i.e., winding angle, respectively. (a) shows the  $\mathcal{A}$  fields of a synthetic 2D steady flow. Their corresponding edges are in (b). (c) shows the  $\mathcal{A}$  fields of a 2D force duffing system.

**FTLE approach vs. accumulating flow vectors along path-lines** In addition to accumulating the scalar quantities along the integral curves, we can accumulate vector-valued properties. The resulting  $\mathcal{A}$  field is then a vector field. We use this vector-valued accumulation to study the relation of the FTLE computation and a derived scalar field computed from an  $\mathcal{A}$  field by accumulating the flow vectors scaled by the integration step size along integral curves. Assuming a forward accumulation is considered, i.e.,  $t > 0$  in Eq.(1), the resulting vector is an orientation vector that points from the starting point to the end point of the integral curve [11], denoted by  $V_{SE}(\mathbf{x}) = \phi_{t_0+t}^{t_0}(\mathbf{x}) - \phi_{t_0}^{t_0}(\mathbf{x})$  using the notation of a flow map [27]. We store this accumulated vector to the corresponding seeding point of the integral curve, resulting in a vector-valued version of the  $\mathcal{A}$  field. It is not difficult to verify that

$$F = \frac{dV_{SE}(\mathbf{x})}{d\mathbf{x}} = \frac{d\phi_{t_0+t}^{t_0}(\mathbf{x})}{d\mathbf{x}} - I_2 \quad (3)$$

where  $\frac{dV_{SE}(\mathbf{x})}{d\mathbf{x}}$  denotes the gradient of the vector-valued  $\mathcal{A}$  field,  $\frac{d\phi_{t_0+t}^{t_0}(\mathbf{x})}{d\mathbf{x}}$  denotes the flow map deformation, and  $I_2$  is an  $2 \times 2$  identity matrix. We then compute  $s_{t_0}'(\mathbf{x}) = \frac{1}{t} \ln \sqrt{\lambda_{\max}(G)}$ , where  $G = F^T F$  is a Cauchy tensor and  $\lambda_{\max}$  is the maximum

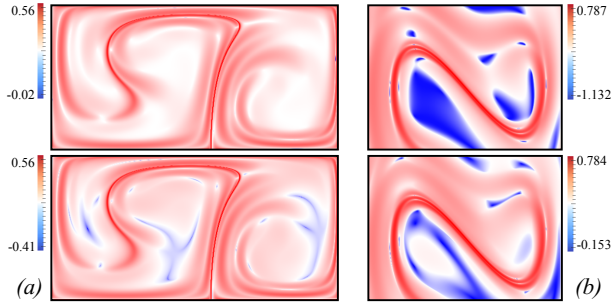


Fig. 10: Comparison of the FTLE fields (top) and a derived fields (bottom) from the  $\mathcal{A}$  fields—vector fields defined by  $V_{SE}$  for the double gyre flow (a) and the force duffing system (b).

eigenvalue of  $G$ . This gives rise to a scalar field that has similar patterns to the corresponding FTLE field computing using the same time window according to Eq.(3). Figure 10 provides a comparison of the original FTLE fields (top) and the derived scalar fields (bottom) from  $V_{SE}$  for a number of 2D unsteady flows. These results suggest that the attribute that quantifies the difference from the starting point to the end point of an integral curve encodes the information regarding flow separation. Nonetheless, the accumulation of vectors using direct vector summation may lead to degeneracy. For instance, accumulating tangent vectors along a closed integral curve results in a zero vector. Therefore, a more appropriate accumulation may be to separate the accumulation of the direction and magnitude components, which requires further investigation.

Similarly, one can use the accumulation to verify the relationship among other vector quantities, such as the difference vector between two consecutive flow vectors along integral curves and the acceleration of the flow. In addition, the Jacobian of the vector field, an asymmetric tensor [43], may be accumulated along the integral curves, which could provide additional insights into the general deformation of the flow particles along their paths. We will leave the detailed discussion of these accumulations to a future work.

**What attribute(s) to accumulate?** Based on existing results in the literature, we observe that if the goal is to study the transport of the flow or the variation of the state of the particles along their paths, then the physical properties are typically selected [36]. On the other hand, for the integral curve dissimilarity computation, their geometric characteristics are usually preferred over their physical properties [30]. However, this should not be treated as a general rule, as demonstrated by a recent work [28] in which the physical properties were also used to define the distance between integral curves. We believe that more in-depth investigation to the accurate relations among attributes is required in the future.

In addition, different local characteristics may be related by physical principles [8]. Nonetheless, we admit that, given certain flow behaviors of interest, there could be more than one characteristic that describes it, and the  $\mathcal{A}$  fields that are computed from different characteristics may encode overlapping information. For specific applications, selection of the appropriate characteristics deserves a detailed and comprehensive dis-

cussion as provided in [8], which is beyond the scope of this work.

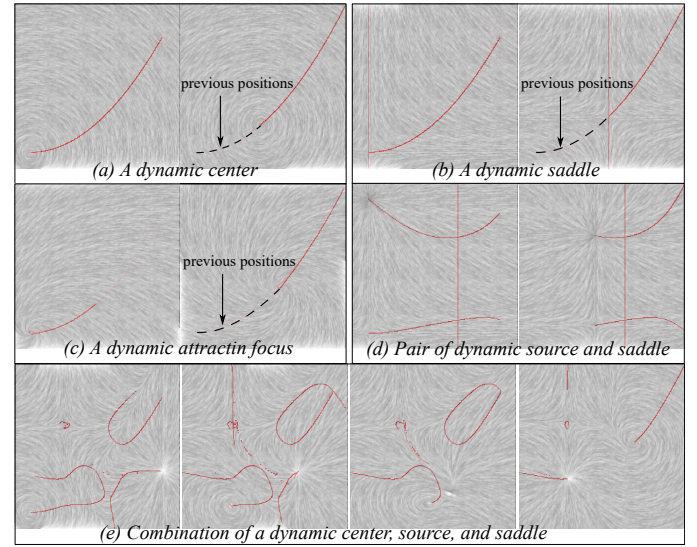


Fig. 11: The  $|\nabla\Phi|$  fields based on streaklines for a number of synthetic unsteady flows.

### 5.3. Extension to Non-integral Curves – Streak Lines

Our accumulation framework for integral curves can be extended to other geometric curves derived from the vector fields, such as streak lines. A *streak line*,  $\tilde{s}(t)$ , is the connection of the current positions of the particles,  $\mathbf{p}_i(t)$ , that are released from position  $p_0$  at consecutive time  $t_i$ . Since the meaning of accumulating physical attributes along a streak line

is yet to be clarified, we concentrate on the local geometric characteristics, such as the curvature or the change of the streak line direction. To reduce the memory overload, we limited the number of particles released for each streak line to 200. This may affect the smoothness of streak lines depending on the time window for the computation. To handle boundaries, we simply terminate the computation of a streak line once any of its particles hit a boundary. The inset shows the result for the Double Gyre flow. From this result, we notice two edge segments in both the  $\mathcal{A}$  field (top) and the  $|\nabla\mathcal{A}|$  field (bottom) (highlighted by the arrows). With a closer look, we find that these two edge segments correspond to the paths of the two oscillating centers. To further verify our conjecture, we perform accumulation along streak lines derived from a number of synthetic unsteady vector fields that possess various moving singularities. Figure 11 shows the results. Not surprisingly, the highlighted ridges in the  $|\nabla\mathcal{A}|$  fields of these examples indeed correspond to the paths of the singularities.

Why does the  $\mathcal{A}$  field computed based on streak links reveal the singularity paths, while the one based on the pathlines cannot? To explain this, let us consider a pathline starting at position  $\mathbf{x}_0$



at time  $t_i$ , which defines a flow map  $\phi_{t_i}^t(\mathbf{x}_0)$ . Once it moves away from  $\mathbf{x}_0$ , information about what happens at  $\mathbf{x}_0$  after  $t_i$  is not encoded in that pathline. In contrast, a streak line starting from  $\mathbf{x}_0$  and perceived at time  $t_j(> t_i)$  is a collection of particles that are released at  $\mathbf{x}_0$  from  $t_i$  to  $t_j$ . Therefore, it naturally encodes the temporal variation of flow maps passing  $\mathbf{x}_0$  after  $t_i$ . As we already showed before, the translation of the singularities will cause the sharp change in the direction of integral curves. This abrupt geometry change is captured by the accumulation for a streak line. Nonetheless, we believe additional effort should be made to provide a more rigorous interpretation of the patterns revealed in the streak line based  $\mathcal{A}$  fields.

#### 5.4. Comparison with the Eulerian Accumulation

To some extent, the above Lagrangian accumulation framework allows us to inspect the aggregated (or overall) behavior of particles during their advection (especially in the unsteady setting). In the meantime, we can accumulate (or aggregate) the attribute values measured at the fixed locations but over time to obtain the overall information of the flow at those locations. This scenario shares some similarity with the way different weather measurements are collected at those fixed stations. We refer to this accumulation the *Eulerian accumulation*.

Figure 12 (a) shows the Eulerian accumulation results of a number of attributes for the 2D flow behind cylinder data. Most of these attributes are relevant to the vortical behaviors of the flow. As the vortex street pattern behind the cylinder in this flow is well known (which is also depicted by the texture image of the original flow minus the ambient component), we can clearly observe that the obtained  $\mathcal{A}$  fields all highlight the regions where the vortices sweep through. In particular, the regions highlighted by the accumulation of acceleration magnitude,  $\lambda_2$  and the determinant of the Jacobian clearly highlight the places that the vortex centers go through, which induce two tails in the later part of the domain (highlighted by the arrows). In contrast, the Lagrangian accumulation of the same attributes (Figure 12 (b)) does not provide this overall aggregated information of vortex regions but rather it highlights the oscillating behavior of the individual vortices.

## 6. Conclusion

In this work, we revisit the Lagrangian accumulation framework for the vector field data exploration. We focus on an in-depth and thorough discussion on the properties of the derived  $\mathcal{A}$  fields based on the accumulated attributes along integral curves. In particular, we study the discontinuity exhibited in the  $\mathcal{A}$  fields and analyze its relation to the flow structure. We conclude that the discontinuity structure in the  $\mathcal{A}$  fields is aligned with the flow direction and can reveal additional discontinuous behaviors in the flow characteristics that cannot be represented by a conventional description of the flow structure. We also point out that the selection of the integration time in the computation of  $\mathcal{A}$  may greatly influence the patterns in  $\mathcal{A}$ , which is similar to the computation of the FTLE field of the

flow. Properly choosing the integration time can reveal different local (or short-term) and global (or long-term) flow behaviors, respectively. Based on these new insights, we further demonstrate how to apply  $\mathcal{A}$  fields to achieve a number of enhanced flow data visualizations and explorations. To demonstrate the flexibility of the accumulation framework, we extend it to the study of streak line behaviors, which enables us to discover interesting relationship between the geometrically discontinuous behavior of streak lines and the paths of moving singularities. Finally, we introduce the Eulerian accumulation that aggregates information at fixed locations over time, which enables us to study the aggregated behaviors of the flow in a different way from the Lagrangian accumulation.

We have demonstrated that the accumulation framework and the derived  $\mathcal{A}$  fields offer a valuable way to present aggregated information that provides an overview of the flow behavior. The derived  $\mathcal{A}$  fields can also be applied to support various flow exploration tasks. As noted by an expert, the accumulation framework “is relatively straightforward; it is conceivable that application scientists would adopt this technique. I make a point of stating this, since some techniques are so convoluted that it seems inconceivable that end users would adopt them; this work is not in this camp.”

**Limitations and future work** However, there are a number of limitations of which the user should be aware. First, even though we have shown that choosing different window sizes for the accumulation may be employed to generate various visualizations, the selection of an appropriate window is highly application-dependent, which may influence both the computational cost and the revealed structures. Similarly, the sampling strategy could affect the information that can be captured by the  $\mathcal{A}$  fields. Second, during the accumulation, the characteristic values may cancel each other. For instance, if one accumulates the change of the flow direction along a symmetric integral curve that has the behavior similar to a sine function, the resulting value can be zero. Third, the discussed accumulation is also a dimensionality reduction process (i.e., reducing the 1D information into a single value), which will surely result in information loss. However, this information loss and a solution for reducing it have not been carefully discussed and left for future investigation. Fourth, there is a lack of a clear physical interpretation of the exploration process based on the derived attribute fields, which we plan to investigate further in the future.

## Acknowledgment

We would like to thank all the anonymous reviewers for their valuable comments. This work is supported by NSF IIS 1553329.

## References

- [1] Edmunds, M, Laramée, RS, Chen, G, Max, N, Zhang, E, Ware, C. Surface-based flow visualization. *Computers & Graphics* 2012;36(8):974–990.

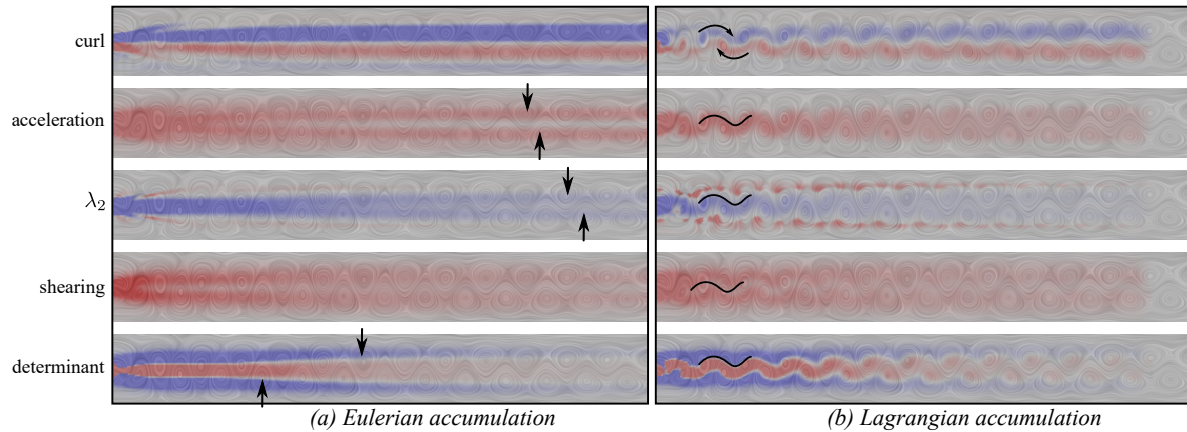


Fig. 12: Comparison of Eulerian (a) and Lagrangian (b) accumulations using various attributes of the flow behind cylinder data. Note that the Eulerian accumulation highlights the places where the vortices sweep through, while the Lagrangian accumulation emphasizes the oscillating behaviors of the individual vortices.

- [2] Laramée, R, Hauser, H, Zhao, L, Post, FH. Topology based flow visualization: the state of the art. In: Topology-Based Methods in Visualization (Proceedings of Topo-in-Vis 2005). Mathematics and Visualization; Springer; 2007, p. 1–19.
- [3] Pobitzer, A, Peikert, R, Fuchs, R, Schindler, B, Kuhn, A, Theisel, H, et al. The state of the art in topology-based visualization of unsteady flow. Computer Graphics Forum 2011;30(6):1789–1811. URL: <http://dx.doi.org/10.1111/j.1467-8659.2011.01901.x>.
- [4] Salzbrunn, T, Wischgoll, T, Jänicke, H, Scheuermann, G. The state of the art in flow visualization: Partition-based techniques. In: Hauser, H, Strassburger, S, Theisel, H, editors. In Simulation and Visualization 2008 Proceedings. SCS Publishing House; 2008, p. 75–92.
- [5] Laramée, RS, Hauser, H, Doleisch, H, Post, FH, Vrolijk, B, Weiskopf, D. The state of the art in flow visualization: dense and texture-based techniques. Computer Graphics Forum 2004;23(2):203–221. URL: <http://www.VRVis.at/ar3/pr2/star/>.
- [6] Matvienko, V, Kruger, J. A metric for the evaluation of dense vector field visualizations. Visualization and Computer Graphics, IEEE Transactions on 2013;19(7):1122–1132.
- [7] Guo, H, Hong, F, Shu, Q, Zhang, J, Huang, J, Yuan, X. Scalable lagrangian-based attribute space projection for multivariate unsteady flow data. In: Pacific Visualization Symposium (PacificVis), 2014 IEEE. IEEE; 2014, p. 33–40.
- [8] Pobitzer, A, Lez, A, Matkovic, K, Hauser, H. A statistics-based dimension reduction of the space of path line attributes for interactive visual flow analysis. In: PacificVis. 2012, p. 113–120.
- [9] Salzbrunn, T, Scheuermann, G. Streamline predicates. IEEE Transactions on Visualization and Computer Graphics 2006;12(6):1601–1612. doi:<http://dx.doi.org/10.1109/TVCG.2006.104>.
- [10] Salzbrunn, T, Garth, C, Scheuermann, G, Meyer, J. Pathline predicates and unsteady flow structures. The Visual Computer 2008;24(12):1039–1051.
- [11] Shi, K, Theisel, H, Hauser, H, Weinkauff, T, Matkovic, K, Hege, HC, et al. Path line attributes - an information visualization approach to analyzing the dynamic behavior of 3D time-dependent flow fields. In: Hege, HC, Polthier, K, Scheuermann, G, editors. Topology-Based Methods in Visualization II. Mathematics and Visualization; Grima, Germany: Springer. ISBN 978-3-540-88605-1; 2009, p. 75–88. doi:10.1007/978-3-540-88606-8\_6.
- [12] Sadarjoen, I, Post, F. Geometric methods for vortex extraction. In: Proc. EG/IEEE Visualization Symposium. 1999,.
- [13] Zhang, L, Laramée, RS, Thompson, D, Sescu, A, Chen, G. Compute and Visualize Discontinuity Among Neighboring Integral Curves of 2D Vector Fields. In: Proceedings of TopoInVis. Germany; 2015,.
- [14] Zhang, L, Chen, G, Laramée, RS, Thompson, D, Sescu, A. Flow visualization based on A derived rotation field. In: Visualization and Data Analysis 2016, San Francisco, California, USA, February 14–18, 2016. 2016, p. 1–10. URL: <http://ist.publisher.ingentaconnect.com/contentone/ist/ei/2016/00002016/00000001/art00004>.
- [15] Zhang, L, Laramée, RS, Thompson, D, Sescu, A, Chen, G. An integral curve attribute based flow segmentation. Journal of Visualization 2016;19(3):423–436.
- [16] McLoughlin, T, Laramée, RS, Peikert, R, Post, FH, Chen, M. Over two decades of integration-based, geometric flow visualization. In: Computer Graphics Forum; vol. 29. Wiley Online Library; 2010, p. 1807–1829.
- [17] Brambilla, A, Carnecky, R, Peikert, R, Viola, I, Hauser, H. Illustrative Flow Visualization: State of the Art, Trends and Challenges. In: Cani, MP, Ganovelli, F, editors. Eurographics 2012 - State of the Art Reports. The Eurographics Association; 2012, p. 75–94. doi:10.2312/conf/EG2012/stars/075-094.
- [18] Cabral, B, Leedom, LC. Imaging vector fields using line integral convolution. In: Proceedings of the 20th annual conference on Computer graphics and interactive techniques. ACM; 1993, p. 263–270.
- [19] Falk, M, Weiskopf, D. Output-sensitive 3d line integral convolution. Visualization and Computer Graphics, IEEE Transactions on 2008;14(4):820–834.
- [20] Huang, J, Pan, Z, Chen, G, Chen, W, Bao, H. Image-space texture-based output-coherent surface flow visualization. Visualization and Computer Graphics, IEEE Transactions on 2013;19(9):1476–1487.
- [21] Shen, HW, Johnson, CR, Ma, KL. Visualizing vector fields using line integral convolution and dye advection. In: Volume Visualization, 1996. Proceedings., 1996 Symposium on. IEEE; 1996, p. 63–70.
- [22] Shen, HW, Kao, DL. Uflic: a line integral convolution algorithm for visualizing unsteady flows. In: Proceedings of the 8th conference on Visualization'97. IEEE Computer Society Press; 1997, p. 317–ff.
- [23] Laramée, RS, van Wijk, JJ, Jobard, B, Hauser, H. Isa and ibfvs: Image space-based visualization of flow on surfaces. IEEE Transactions on Visualization and Computer Graphics 2004;10(6):637–648. URL: <http://dx.doi.org/10.1109/TVCG.2004.47>. doi:10.1109/TVCG.2004.47.
- [24] Van Wijk, JJ. Spot noise texture synthesis for data visualization. In: ACM Siggraph Computer Graphics; vol. 25. ACM; 1991, p. 309–318.
- [25] van Wijk, JJ. Image based flow visualization. In: ACM Transactions on Graphics (SIGGRAPH 02); vol. 21. 2002, p. 745–754.
- [26] Park, SW, Yu, H, Hotz, I, Kreylos, O, Linsen, L, Hamann, B. Structure-accentuating dense flow visualization. In: EuroVis. Citeseer; 2006, p. 163–170.
- [27] Haller, G. Lagrangian coherent structures and the rate of strain in two-dimensional turbulence. Phys Fluids A 2001;13:3365–3385.
- [28] Guo, H, Zhang, J, Liu, R, Liu, L, Yuan, X, Huang, J, et al. Advection-based sparse data management for visualizing unsteady flow. Visualization and Computer Graphics, IEEE Transactions on 2014;20(12):2555–2564.
- [29] Yu, H, Wang, C, Shene, CK, Chen, JH. Hierarchical streamline bundles. IEEE Transactions on Visualization and Computer Graphics 2012;18(8):1353–1367. URL: <http://dx.doi.org/10.1109/TVCG.2011.155>. doi:10.1109/TVCG.2011.155.
- [30] McLoughlin, T, Jones, MW, Laramée, RS, Malki, R, Masters, I, Hansen, CD. Similarity measures for enhancing interactive streamline seeding. IEEE Transactions on Visualization and Computer Graphics 2013;19(8):1342–1353.

- [31] Guo, H, Yuan, X, Huang, J, Zhu, X. Coupled ensemble flow line advection and analysis. Visualization and Computer Graphics, IEEE Transactions on 2013;19(12):2733–2742.
- [32] Chandler, J, Obermaier, H, Joy, K. Interpolation-based pathline tracing in particle-based flow visualization. IEEE Transactions on Visualization and Computer Graphics 2015;21(1):68–80.
- [33] Chen, G, Mischaikow, K, Laramée, RS, Pilarczyk, P, Zhang, E. Vector field editing and periodic orbit extraction using Morse decomposition. IEEE Transactions on Visualization and Computer Graphics 2007;13(4):769–785.
- [34] Jeong, J, Hussain, F. On the identification of a vortex. Journal of fluid mechanics 1995;285:69–94.
- [35] Hunt, JC, Wray, A, Moin, P. Eddies, streams, and convergence zones in turbulent flows. In: Studying Turbulence Using Numerical Simulation Databases, 2; vol. 1. 1988, p. 193–208.
- [36] Shi, K, Theisel, H, Weinkauff, T, Hege, HC, Seidel, HP. Visualizing transport structures of time-dependent flow fields. IEEE Computer Graphics and Applications 2008;28(5):24–36.
- [37] Weinkauff, T, Theisel, H, Sorkine, O. Cusps of characteristic curves and intersection-aware visualization of path and streak lines. In: Peikert, R, Hauser, H, Carr, H, Fuchs, R, editors. Topological Methods in Data Analysis and Visualization II. Mathematics and Visualization; Springer; 2012, p. 161–176. URL: <http://tinoweinkauff.net/publications/absweinkauff12b.html>.
- [38] Okada, A, Kao, DL. Enhanced line integral convolution with flow feature detection. In: Electronic Imaging'97. International Society for Optics and Photonics; 1997, p. 206–217.
- [39] Skraba, P, Wang, B, Chen, G, Rosen, P. 2d vector field simplification based on robustness. In: Pacific Visualization Symposium (PacificVis), 2014 IEEE. IEEE; 2014, p. 49–56.
- [40] Chen, Y, Cohen, JD, Krolik, J. Similarity-guided streamline placement with error evaluation. IEEE Trans Vis Comput Graph 2007;13(6):1448–1455.
- [41] Roth, M. Automatic extraction of vortex core lines and other line type features for scientific visualization. Hartung-Gorre; 2000.
- [42] Macklin, M, Müller, M. Position based fluids. ACM Trans Graph 2013;32(4):104:1–104:12. URL: <http://doi.acm.org/10.1145/2461912.2461984>. doi:10.1145/2461912.2461984.
- [43] Zhang, E, Yeh, H, Lin, Z, Laramée, RS. Asymmetric tensor analysis for flow visualization. IEEE Transactions on Visualization and Computer Graphics 2009;15(1):106–122.